Crystal structure of brimonidine hydrogen tartrate, $(C_{11}H_{11}BrN_5)(HC_4H_4O_6)$

James A. Kaduk [1,2,a], Anja Dosen [3] and Thomas N. Blanton [3]
[1]*Illinois Institute of Technology, 3101 S. Dearborn St., Chicago, IL 60616, USA*
[2]*North Central College, 131 S. Loomis St., Naperville, IL 60540, USA*
[3]*ICDD, 12 Campus Blvd., Newtown Square, PA 19073-3273, USA*

(Received 9 December 2023; accepted 20 March 2024)

The crystal structure of brimonidine hydrogen tartrate has been solved and refined using synchrotron X-ray powder diffraction data and optimized using density functional techniques. Brimonidine hydrogen tartrate crystallizes in space group $P2_1$ (#4) with $a = 7.56032(2)$, $b = 7.35278(2)$, $c = 30.10149(9)$ Å, $\beta = 90.1992(2)°$, $V = 1673.312(10)$ Å^3, and $Z = 4$ at 295 K. The crystal structure consists of alternating layers of cations and anions parallel to the *ab*-plane. Each of the hydrogen tartrate anions is linked to itself by very strong charge-assisted O–H···O hydrogen bonds into chains along the *a*-axis. Each hydroxyl group of each tartrate acts as a donor in an O–H···O or O–H···N hydrogen bond. One of these is intramolecular, but the other three are intermolecular. These hydrogen bonds link the hydrogen tartrate anions into layers parallel to the *ab*-plane and also link the anion–cation layers. The protonated N atoms act as donors in N–H···O or N–H···N hydrogen bonds to the carboxyl groups of the tartrates and to a ring nitrogen atom. These link the cations and anions, as well as providing cation–cation links. The amino N atoms of the cations form N–H···O hydrogen bonds to hydroxyl groups of the anions. The powder pattern has been submitted to ICDD for inclusion in the Powder Diffraction File™ (PDF®)

[doi:10.1017/S0885715624000174]

Key words: brimonidine, alphagan, powder diffraction, Rietveld refinement, density functional theory

I. INTRODUCTION

Brimonidine tartrate (marketed under the trade names Alphagan and Qoliana) is administered as a dilute aqueous solution used for lowering the intraocular pressure in patients with glaucoma or ocular hypertension. The systematic name (CAS Registry Number 70359-46-5) is 5-bromo-N-(4,5-dihydro-1H-imidazol-2-yl)quinoxalin-6-amine (2R,3R)-2,3-dihydroxybutanedioic acid. A two-dimensional molecular diagram of brimonidine hydrogen tartrate is shown in Figure 1.

Limited powder diffraction data for a novel Form A polymorph of brimonidine tartrate is reported in Japanese patent JP6270603 B2 (Kanazawa, 2018; Kasuma Partners Inc.). A powder pattern for brimonidine tartrate is contained in De Souza et al. (2016); however, the crystal structure was not reported.

This work was carried out as part of a project (Kaduk et al., 2014) to determine the crystal structures of large-volume commercial pharmaceuticals and include high-quality powder diffraction data for them in the Powder Diffraction File (Gates-Rector and Blanton, 2019).

II. EXPERIMENTAL

Brimonidine tartrate was a commercial reagent, purchased from TargetMol (Batch #115202), and was used as received. The white powder was packed into a 1.5 mm diameter Kapton capillary and rotated during the measurement at ~50 Hz. The powder pattern was measured at 295 K at beam line 11-BM (Antao et al., 2008; Lee et al., 2008; Wang et al., 2008) of the Advanced Photon Source at Argonne National Laboratory using a wavelength of

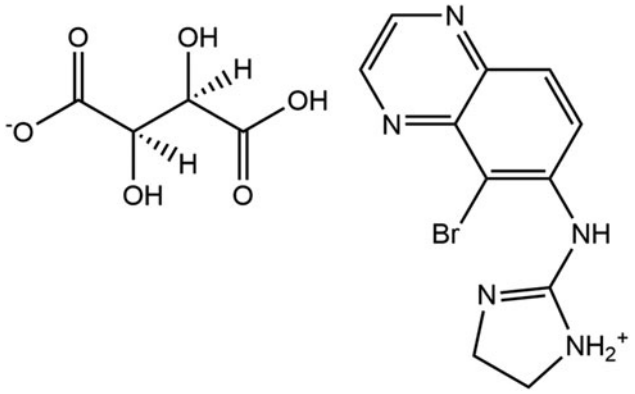

Figure 1. The two-dimensional structure of brimonidine hydrogen tartrate.

[a]Author to whom correspondence should be addressed. Electronic mail: kaduk@polycrystallography.com

0.459744(2) Å from 0.5 to 40° 2θ with a step size of 0.001° and a counting time of 0.1 s/step. The high-resolution powder diffraction data were collected using 12 silicon crystal analyzers that allow for high angular resolution, high precision, and accurate peak positions. A mixture of silicon (NIST SRM 640c) and alumina (NIST SRM 676a) standards (ratio Al_2O_3:Si = 2:1 by weight) was used to calibrate the instrument and refine the monochromatic wavelength used in the experiment.

The pattern was indexed using N-TREOR (Altomare et al., 2013) on a primitive monoclinic unit cell with $a = 7.70622$, $b = 7.36944$, $c = 30.43616$ Å, $\beta = 91.311°$, $V = 1728.0$ Å^3, and $Z = 4$. The suggested space group was $P2_1$, which was confirmed by the successful solution and refinement of the structure. A reduced cell search of the Cambridge Structural Database (Groom et al., 2016) with the chemistry C, H, Br, N, and O only, yielded no hits.

The brimonidine molecule was downloaded from PubChem (Kim et al., 2023) as Conformer3D_CID_2435.sdf. It was converted to a *.mol2 file using Mercury (Macrae et al., 2020). The tartrate.mol2 file used in the solution of the structure of varenicline hydrogen tartrate (Kaduk et al., 2021) was used as the tartrate model. The crystal structure was solved using Monte Carlo simulated annealing techniques as implemented in EXPO2014 (Altomare et al., 2013), using two brimonidine and two tartrate molecules as the fragments (37 variables), including a default bump penalty for the non-H atoms.

Examining potential hydrogen bonds in the best solution made it clear that N4 and N30 in the two cations were protonated, and that O57 and O75 in the tartrate anions were also protonated (Figure 2). Hydrogen atoms were added to these N and O atoms in approximate positions. The bulk stoichiometry is a 1:1 salt, and the tartrate anions are monoionized, so the compound is best described as brimonidine hydrogen tartrate.

Rietveld refinement was carried out with GSAS-II (Toby and Von Dreele, 2013). Only the 0.8–32.0° portion of the pattern was included in the refinements ($d_{min} = 0.834$ Å). The y-coordinate of Br1 was fixed to define the origin. All non-H bond distances and angles were subjected to restraints, based on a Mercury/Mogul Geometry Check (Bruno et al., 2004; Sykes et al., 2011). The Mogul average and standard deviation for each quantity were used as the restraint parameters. The imidazole rings and the fused ring systems in the two independent brimonidine cations were restrained to be planar. The restraints contributed 7.8% to the final χ^2. The hydrogen atoms were included in calculated positions, which were recalculated during the refinement using Materials Studio (Dassault, 2022). The two independent Br atoms were refined anisotropically. The U_{iso} of the C, N, and O atoms were grouped by chemical similarity. The U_{iso} for the H atoms was fixed at 1.3× the U_{iso} of the heavy atoms to which they are attached. The peak profiles were described using a uniaxial microstrain model, with 001 as the unique axis.

The final refinement of 198 variables using 31,250 observations and 136 restraints yielded the residuals $R_{wp} = 0.09075$ and goodness of fit (GOF) = 1.63. The largest peak (1.59 Å from Br1) and hole (1.43 Å from C37) in the difference Fourier map were 0.51(11) and −0.49(16) eÅ^{-3}, respectively. The final Rietveld plot is shown in Figure 3. The largest features in the normalized error plot represent subtle shifts in peak positions and may represent a change to the specimen during the measurement.

The crystal structure of brimonidine hydrogen tartrate was optimized (fixed experimental unit cell) with density functional techniques using Vienna Ab initio Simulation Package (VASP) (Kresse and Furthmüller, 1996) through the MedeA graphical interface (Materials Design, 2016). The calculation was carried out on 16 2.4 GHz processors (each with 4 Gb RAM) of a 64-processor HP Proliant DL580 Generation 7 Linux cluster at North Central College. The calculation used the generalized gradient approximation-Perdew-Burke-Ernzerhof (GGA-PBE) functional, a plane wave cutoff energy of 400.0 eV, and a k-point spacing of 0.5 Å^{-1} leading to a 2 × 2 × 1 mesh, and took ~38 h. Single-point density functional calculations (fixed experimental cell) and population analysis were carried out using CRYSTAL23 (Erba et al., 2023). The basis sets for the H, C, N, and O atoms in the calculation were those of Gatti

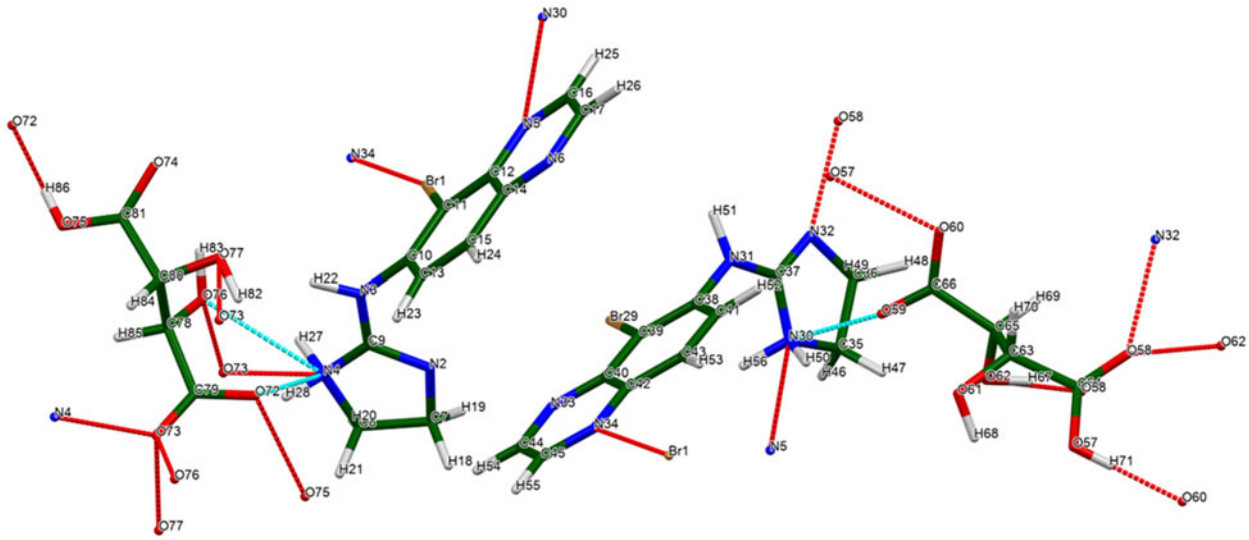

Figure 2. Potential hydrogen bonds in brimonidine hydrogen tartrate, which suggested the locations of the active hydrogen atoms.

https://doi.org/10.1017/S0885715624000174 Published online by Cambridge University Press

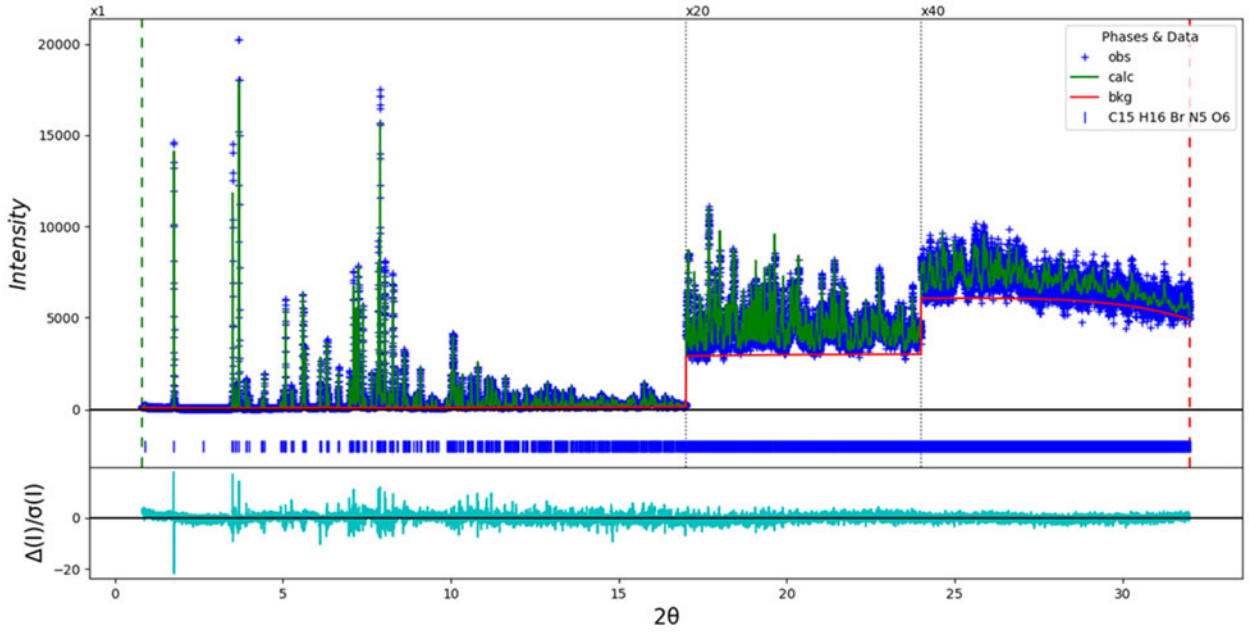

Figure 3. The Rietveld plot for the refinement of brimonidine hydrogen tartrate. The blue crosses represent the observed data points, and the green line is the calculated pattern. The cyan curve is the normalized error plot, and the red line is the background curve. The vertical scale has been multiplied by a factor of 20× for $2\theta > 17.0$° and by a factor of 40× for $2\theta > 24.0$°.

et al. (1994), and the basis set for Br was that of Peintinger et al. (2013). The calculations were run on a 3.5 GHz personal computer (PC) using 8 *k*-points and the B3LYP functional and took ∼5.1 h.

III. RESULTS AND DISCUSSION

The limited powder data (four peaks) reported by Kanazawa (2018; Table I, Figure 4) makes it difficult to conclude that our material and the "novel polymorph" claimed by Kasuma are the same. The agreement of the third peak in the patent with our pattern is poor, suggesting that the "novel polymorph" claimed there was indeed new. The agreement of our pattern with that reported by De Souza et al. (2016) is quite good (Figure 5), suggesting that the two materials are the same.

The asymmetric unit (Figure 6) contains two brimonidine cations and two hydrogen tartrate anions, showing that the compound should be properly described as brimonidine hydrogen tartrate. The root-mean-square Cartesian displacements of the non-H atoms in the Rietveld-refined and VASP-optimized cations molecules are 0.241 and 0.240 Å (Figures 7 and 8). The agreement is within the normal range for correct structures (van de Streek and Neumann, 2014). The comparable differences for the tartrate anions are 0.099 and 0.484 Å. The difference in anion 2 is mainly the result of different orientations of the C81–O74–O5 carboxyl group. The remainder of this discussion will emphasize the VASP-optimized structure.

Most of the bond distances, bond angles, and torsion angles fall within the normal ranges indicated by a Mercury Mogul Geometry check (Macrae et al., 2020). Exceptions are the C9–N3 distance of 1.351 Å (average = 1.385(11) Å, *Z*-score = 3.1), the C9–N4 distance of 1.512 Å (average = 1.338(52) Å, *Z*-score = 3.4), the C37–N30 distance of 1.510 Å (average = 1.338(52) Å, *Z*-score = 3.4), and the C37–N31 distance of 1.356 Å (average = 1.385(11) Å, *Z*-score = 3.1). These distances represent the differences between the protonated NH_2 and the N = in the imidazole

TABLE I. Powder pattern of brimonidine tartrate Form A from JP6270603B2

2θ (Cu K_α),°	I_{rel}	*d*-spacing, Å	2θ ($\lambda = 0.459744$),°
11.87	>5	7.4497	3.536
12.48	>1.7	7.0869	3.717
20.04	>1.8	4.4272	5.952
34.3	1	2.6123	10.096

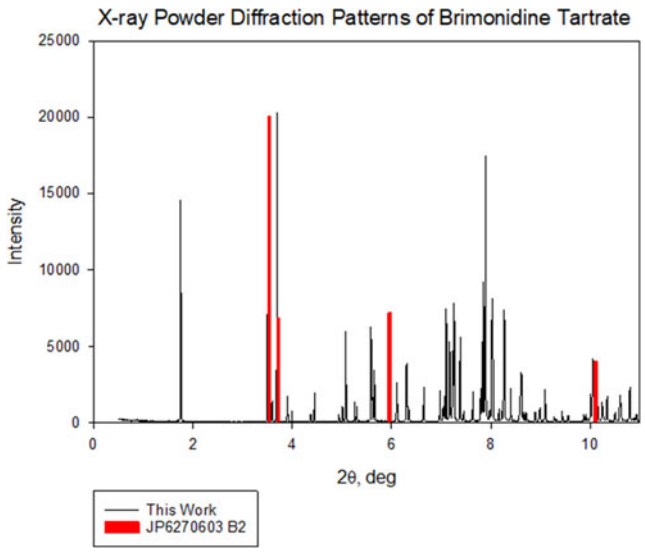

Figure 4. Comparison of this synchrotron powder pattern of brimonidine hydrogen tartrate with peak positions reported in Japanese Patent JP6270603 B2 (Kanazawa, 2018).

https://doi.org/10.1017/S0885715624000174 Published online by Cambridge University Press

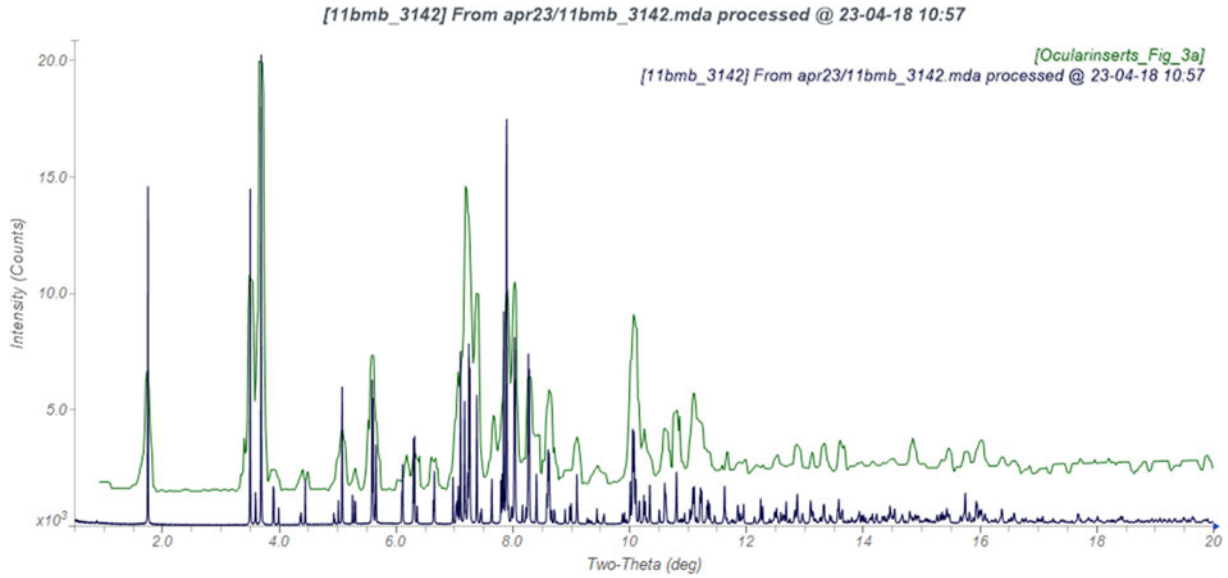

Figure 5. Comparison of the synchrotron pattern of brimonidine hydrogen tartrate (black) to that reported by De Souza et al. (2016; green). The literature pattern (measured using Cu K_α radiation) was digitized using UN-SCAN-IT (Silk Scientific, 2013) and converted to the synchrotron wavelength of 0.459744(2) Å using JADE Pro (MDI, 2023). Image generated using JADE Pro (MDI, 2023).

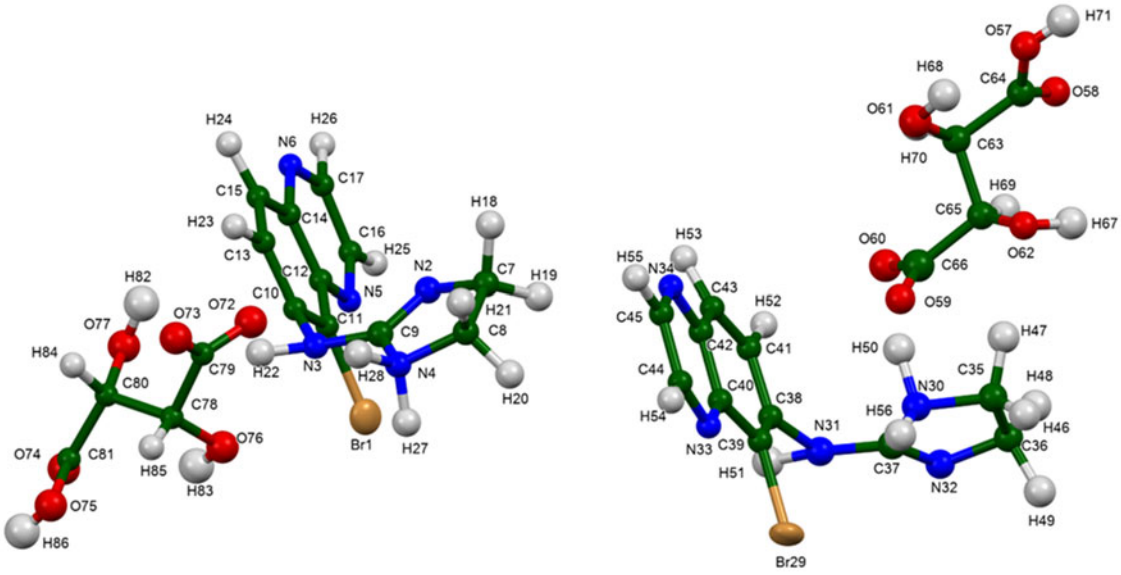

Figure 6. The asymmetric unit of brimonidine hydrogen tartrate, with the atom numbering. The atoms are represented by 50% probability spheroids/ellipsoids. Image generated using Mercury (Macrae et al., 2020).

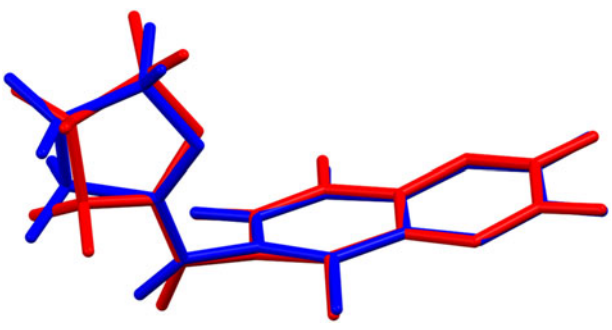

Figure 7. Comparison of the Rietveld-refined (red) and VASP-optimized (blue) structures of cation 1 in brimonidine hydrogen tartrate. The rms Cartesian displacement is 0.241 Å. Image generated using Mercury (Macrae et al., 2020).

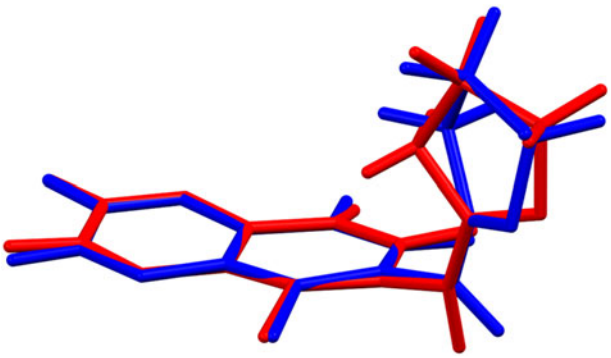

Figure 8. Comparison of the Rietveld-refined (red) and VASP-optimized (blue) structures of cation 2 in brimonidine hydrogen tartrate. The rms Cartesian displacement is 0.240 Å. Image generated using Mercury (Macrae et al., 2020).

https://doi.org/10.1017/S0885715624000174 Published online by Cambridge University Press

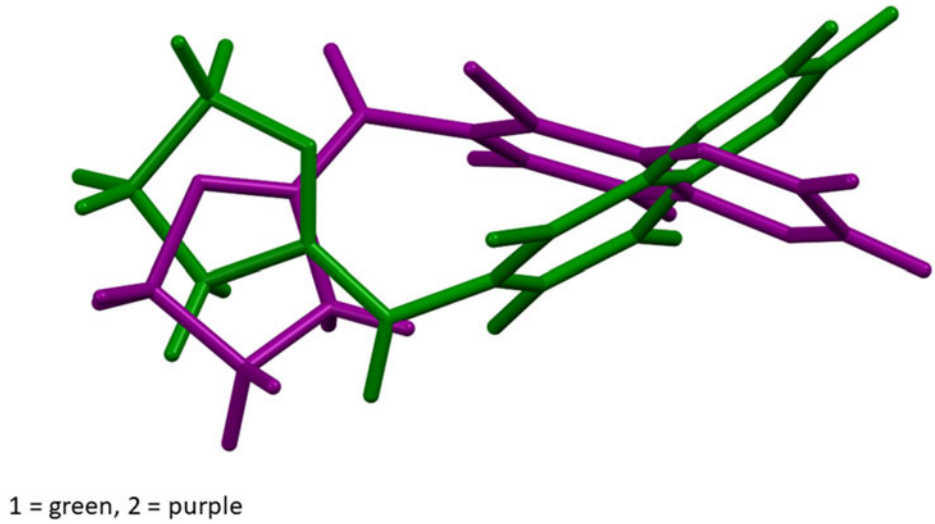

Figure 9. Comparison of cation 1 (green) and cation 2 (purple) in brimonidine hydrogen tartrate. Image generated using Mercury (Macrae et al., 2020).

rings of the cations. The orientations of the hydrogen bonds show that these groups are assigned correctly, and that the rings are not rotated by 180° (which would yield less-reasonable hydrogen bonds). The C10–N3–C9 angle of 117.2° (average = 127.2(24)°, *Z*-score = 4.2) is flagged as unusual. The torsion angles involving rotation about the C9–C3 and C37–N31 bonds are flagged as unusual. These reflect the orientations of the protonated imidazole rings with respect to the fused ring systems and lie on the tails of 0/180° distributions of similar torsion angles. The protonation of the imidazole rings and the resulting hydrogen bonds to the tartrate anions result in unusual geometries for the brimonidine cations.

The two cations have different conformations (Figure 9). The rms Cartesian displacement is 1.708 Å, and after inverting one of them the difference decreases to 0.861 Å. The main

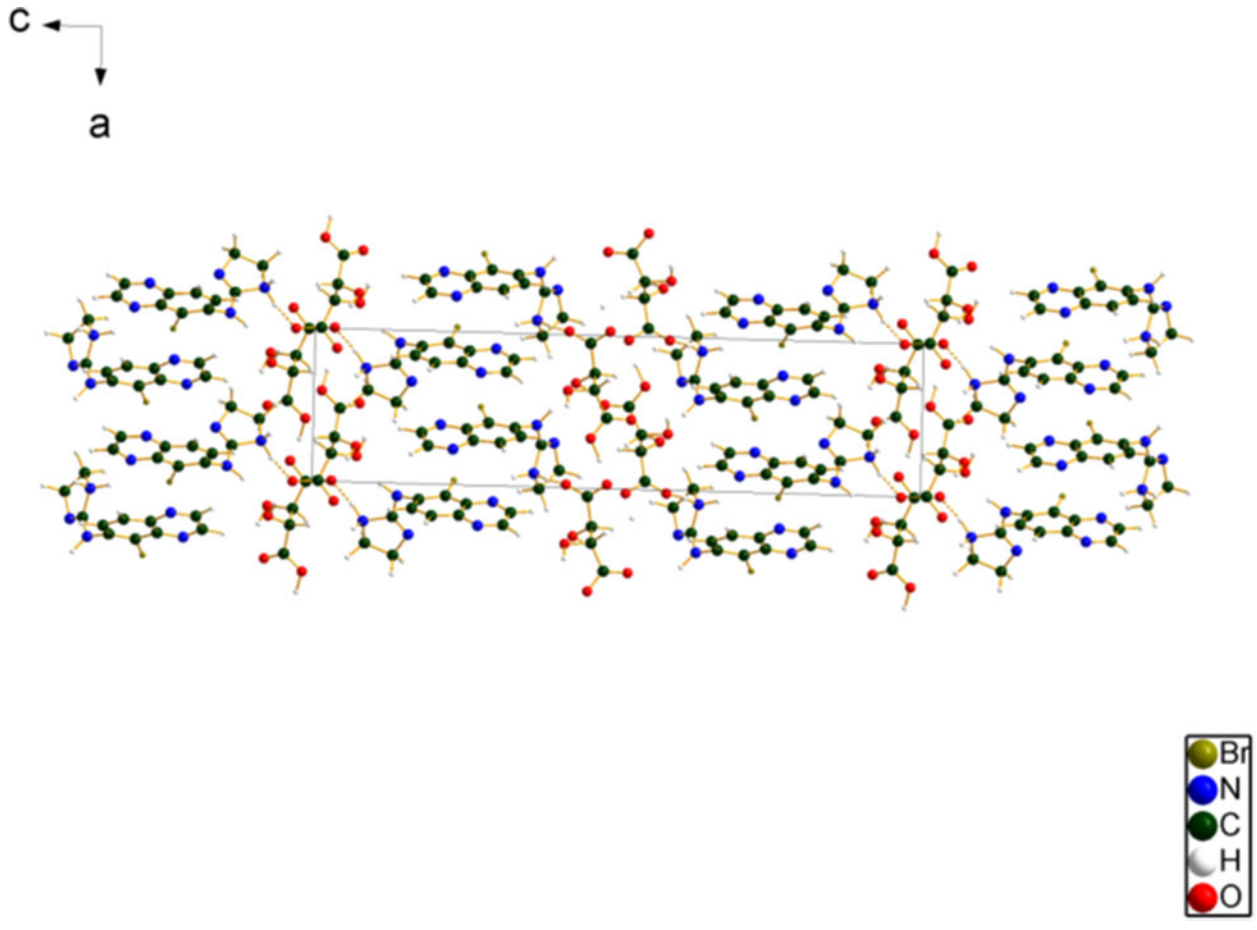

Figure 10. The crystal structure of brimonidine hydrogen tartrate, viewed down the *b*-axis. Image generated using Diamond (Crystal Impact, 2023).

https://doi.org/10.1017/S0885715624000174 Published online by Cambridge University Press

TABLE II. Hydrogen bonds (CRYSTAL23) in brimonidine hydrogen tartrate

H-Bond	D–H, Å	H···A, Å	D···A, Å	D–H···A,◦	Overlap, *e*	*E*, kcal/mol
O57–H71···O60	1.166	1.286	2.446	172.4	0.127	19.5
O75–H86···O72	1.142	1.286	2.422	172.0	0.117	18.7
O62–H67···O58	1.003	1.661	2.648	166.8	0.064	13.8
O61–H68···N32	0.985	2.397	3.351	162.8	0.029	
O77–H82···O73	0.991	1.824	2.812	174.2	0.051	12.3
O76–H83···O74	0.989	1.873[a]	2.719	141.8	0.046	11.7
C65–H69···O57	1.101	2.556	3.518	145.3	0.010	
C78–H85···O75	1.105	2.233	3.264	154.4	0.018	
N4–H27···O73	1.055	1.764	2.803	167.6	0.074	6.3
N4–H28···O74	1.045	1.940	2.848	143.3	0.054	5.4
N30–H50···O59	1.088	1.504	2.585	171.5	0.094	7.1
N30–H56···N5	1.049	2.007	2.914	142.9	0.061	
N3–H22···O76	1.033	1.820	2.812	159.7	0.059	5.6
N31–H51···O62	1.037	1.852	2.888	177.2	0.075	6.3
C15–H24···N2	1.090	2.913	3.263	166.7	0.023	
C16–H25···O59	1.091	2.149	3.102	144.4	0.029	
C17–H26···O61	1.091	2.369	3.196	131.3	0.015	
C41–H52···O57	1.090	2.411	3.485	168.1	0.019	
C44–H54···O74	1.093	2.490	3.535	159.6	0.014	
C8–H21···O75	1.094	2.442	3.473	156.5	0.018	
C35–H47···O62	1.095	2.736	3.655	141.2	0.012	
C36–H48···O60	1.102	2.584	3.672	169.0	0.018	
C36–H49···O59	1.095	2.459	3.504	159.0	0.016	

[a]Intramolecular.

differences after inversion are in the protonated imidazole rings. Quantum chemical geometry optimization of the isolated cations (DFT/B3LYP/6-31G*/water) using Spartan '20 (Wavefunction, 2022) indicated that the cation 1 is 2.2 kcal/mol lower in energy. The global minimum-energy conformation of the cation differs only slightly from the observed conformations. The conformations of the isolated tartrate anions differ by 3.3 kcal/mol (tartrate #1 is lower), reflecting the differences in the hydrogen bonding.

The crystal structure (Figure 10) consists of alternating layers of cations and anions parallel to the *ab*-plane. The mean planes of the fused ring systems are 7,3,1 and 12,5,–1. The Mercury Aromatics Analyser indicates moderate and weak interactions between the fused ring systems, with distances of 4.54 and 4.70 Å, respectively. Manual analysis indicates two even shorter interactions of 3.50 and 3.60 Å between the C_6 and C_4N_2 rings in adjacent molecules, reflecting the parallel stacking of the rings along the *a*-axis. Analysis of the contributions to the total crystal energy of the structure using the Forcite module of Materials Studio (Dassault Systèmes, 2022) suggests that angle and torsion distortion terms dominate the intramolecular deformation energy. The intermolecular energy is dominated by electrostatic repulsions.

Hydrogen bonds are important in the crystal structure (Table II). Each of the hydrogen tartrate anions is linked to itself by very strong charge-assisted O–H···O hydrogen bonds into chains along the *a*-axis. Each hydroxyl group of each tartrate acts as a donor in an O–H···O or O–H···N hydrogen bond. One of these is intramolecular, but the other three are intermolecular. These hydrogen bonds link the hydrogen tartrate anions into layers parallel to the *ab*-plane and also link the anion–cation layers. The protonated N atoms N4 and N30 act as donors in N–H···O or N–H···N hydrogen bonds, to the carboxyl groups of the tartrates and to a ring nitrogen atom. These link the cations and anions, as well as providing cation–cation links. The amino N atoms N3 and H31 form N–H···O hydrogen bonds to hydroxyl groups of the anions. The energies of the O–H···O hydrogen bonds were calculated using the correlation of Rammohan and Kaduk (2018) and those of the N–H···O hydrogen bonds by the correlation of Wheatley and Kaduk (2019). Several C–H···O/N hydrogen bonds, both from the cations and anions, also contribute to the lattice energy.

The volume enclosed by the Hirshfeld surface of brimonidine hydrogen tartrate (Figure 11, Hirshfeld, 1977; Spackman et al., 2021) is 825.55 $Å^3$, 98.67% of the unit cell volume. The packing density is thus fairly typical. The only significant close contacts (red in Figure 11) involve the hydrogen

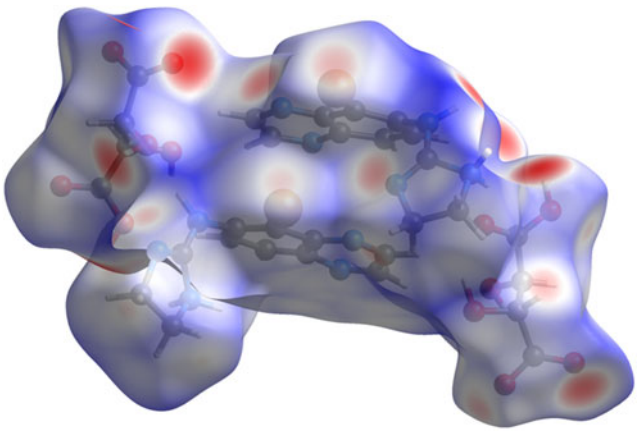

Figure 11. The Hirshfeld surface of brimonidine hydrogen tartrate. Intermolecular contacts longer than the sums of the van der Waals radii are colored blue, and contacts shorter than the sums of the radii are colored red. Contacts equal to the sums of radii are white. Image generated using CrystalExplorer (Spackman et al., 2021).

https://doi.org/10.1017/S0885715624000174 Published online by Cambridge University Press

bonds. The volume/non-hydrogen atom is smaller than normal, at 15.5 $Å^3$, reflecting the extensive hydrogen bonding.

The Bravais–Friedel–Donnay–Harker (Bravais, 1866; Friedel, 1907; Donnay and Harker, 1937) morphology suggests that we might expect platy morphology for brimonidine hydrogen tartrate, with {001} as the major faces. A second-order spherical harmonic model was included in the refinement. The texture index was 1.014(0), indicating that the preferred orientation was not significant in this rotated capillary specimen.

IV. DEPOSITED DATA

The powder pattern of brimonidine hydrogen tartrate from this synchrotron data set has been submitted to ICDD for inclusion in the Powder Diffraction File. The Crystallographic Information Framework (CIF) files containing the results of the Rietveld refinement (including the raw data) and the DFT geometry optimization were deposited with the ICDD. The data can be requested at pdj@icdd.com.

ACKNOWLEDGEMENTS

Use of the Advanced Photon Source at Argonne National Laboratory was supported by the U. S. Department of Energy, Office of Science, Office of Basic Energy Sciences, under Contract No. DE-AC02-06CH11357. This work was partially supported by the International Centre for Diffraction Data. We thank Saul Lapidus for his assistance in the data collection.

CONFLICTS OF INTEREST

The authors have no conflicts of interest to declare.

REFERENCES

Altomare, A., C. Cuocci, C. Giacovazzo, A. Moliterni, R. Rizzi, N. Corriero, and A. Falcicchio. 2013. "EXPO2013: A Kit of Tools for Phasing Crystal Structures from Powder Data." *Journal of Applied Crystallography* 46: 1231–5.

Antao, S. M., I. Hassan, J. Wang, P. L. Lee, and B. H. Toby. 2008. "State-of-the-Art High-Resolution Powder X-Ray Diffraction (HRPXRD) Illustrated with Rietveld Refinement of Quartz, Sodalite, Tremolite, and Meionite." *Canadian Mineralogist* 46: 1501–9.

Bravais, A. 1866. *Etudes Cristallographiques*. Paris, Gauthier Villars.

Bruno, I. J., J. C. Cole, M. Kessler, J. Luo, W. D. S. Motherwell, L. H. Purkis, B. R. Smith, R. Taylor, R. I. Cooper, S. E. Harris, and A. G. Orpen. 2004. "Retrieval of Crystallographically-Derived Molecular Geometry Information." *Journal of Chemical Information and Computer Sciences* 44: 2133–44.

Crystal Impact. 2023. Diamond. V. 5.0.0. Crystal Impact - Dr. H. Putz & Dr. K. Brandenburg. Windows.

Dassault Systèmes. 2022. *Materials Studio 2023*. San Diego, CA, BIOVIA.

De Souza, J. F., K. N. Maia, P. S. De Oliveira Patricio, G. M. Fernandes-Cunha, M. G. Da Silva, C. E. De Matos Jensen, and G. Rodrigues Da Silva. 2016. "Ocular inserts based on chitosan and brimonidine tartrate: Development, characterization and biocompatibility." *Journal of Drug Delivery Science and Technology* 32: 21–30.

Donnay, J. D. H., and D. Harker. 1937. "A New Law of Crystal Morphology Extending the Law of Bravais." *American Mineralogist* 22: 446–47.

Erba, A., J. K. Desmarais, S. Casassa, B. Civalleri, L. Donà, I. J. Bush, B. Searle, L. Maschio, L.-E. Daga, A. Cossard, C. Ribaldone, E. Ascrizzi, N. L. Marana, J.-P. Flament, and B. Kirtman. 2023. "CRYSTAL23: A Program for Computational Solid State Physics and Chemistry." *Journal of Chemical Theory and Computation* 19: 6891–932. doi:10.1021/acs.jctc.2c00958.

Friedel, G. 1907. "Etudes sur la loi de Bravais." *Bulletin de la Société Française de Minéralogie* 30: 326–455.

Gates-Rector, S., and T. N. Blanton. 2019. "The Powder Diffraction File: A Quality Materials Characterization Database." *Powder Diffraction* 39: 352–60.

Gatti, C., V. R. Saunders, and C. Roetti. 1994. "Crystal-Field Effects on the Topological Properties of the Electron-Density in Molecular Crystals - the Case of Urea." *Journal of Chemical Physics* 101, 10686–96.

Groom, C. R., I. J. Bruno, M. P. Lightfoot, and S. C. Ward. 2016. "The Cambridge Structural Database." *Acta Crystallographica Section B: Structural Science, Crystal Engineering and Materials* 72: 171–9.

Hirshfeld, F. L. 1977. "Bonded-Atom Fragments for Describing Molecular Charge Densities." *Theoretica Chemica Acta* 44: 129–38.

Kaduk, J. A., C. E. Crowder, K. Zhong, T. G. Fawcett, and M. R. Suchomel. 2014. "Crystal Structure of Atomoxetine Hydrochloride (Strattera), $C_{17}H_{22}NOCl$." *Powder Diffraction* 29: 269–73.

Kaduk, J. A., A. M. Gindhart, and T. N. Blanton. 2021. "Powder X-Ray Diffraction of Varenicline Hydrogen Tartrate Form B (Chantix®), $(C_{13}H_{14}N_3)(HC_4H_4O_6)$." *Powder Diffraction* 36: 202–4.

Kanazawa, H. 2018. "Novel Polymorph of Brimonidine Tartrate and Process for Producing the Same." Japanese Patent JP6270603 B2.

Kim, S., J. Chen, T. Cheng, A. Gindulyte, J. He, S. He, Q. Li, B. A. Shoemaker, P. A. Thiessen, B. Yu, L. Zaslavsky, J. Zhang, and E. E. Bolton. 2023. "Pubchem 2023 Update." *Nucleic Acids Research* 51 (D1): D1373–80. doi:10.1093/nar/gkac956.

Kresse, G., and J. Furthmüller. 1996. "Efficiency of Ab-Initio Total Energy Calculations for Metals and Semiconductors Using a Plane-Wave Basis Set." *Computational Materials Science* 6: 15–50.

Lee, P. L., D. Shu, M. Ramanathan, C. Preissner, J. Wang, M. A. Beno, R. B. Von Dreele, L. Ribaud, C. Kurtz, S. M. Antao, X. Jiao, and B. H. Toby. 2008. "A Twelve-Analyzer Detector System for High-Resolution Powder Diffraction." *Journal of Synchrotron Radiation* 15: 427–32.

Macrae, C. F., I. Sovago, S. J. Cottrell, P. T. A. Galek, P. McCabe, E. Pidcock, M. Platings, G. P. Shields, J. S. Stevens, M. Towler, and P. A. Wood. 2020. "*Mercury 4.0*: From Visualization to Design and Prediction." *Journal of Applied Crystallography* 53: 226–35.

Materials Design. 2016. *MedeA 2.20.4*. Angel Fire, NM, Materials Design Inc.

MDI. 2023. *JADE Pro Version 8.3*. Livermore, CA, Materials Data.

Peintinger, M. F., D. Vilela Oliveira, and T. Bredow. 2013. "Consistent Gaussian Basis Sets of Triple-Zeta Valence with Polarization quality for Solid-State Calculations." *Journal of Computational Chemistry* 34: 451–9.

Rammohan, A., and J. A. Kaduk. 2018. "Crystal Structures of Alkali Metal (Group 1) Citrate Salts." *Acta Crystallographica Section B: Crystal Engineering and Materials* 74: 239–52. doi:10.1107/S2052520618002330.

Silk Scientific. 2013. *UN-SCAN-IT 7.0*. Orem, UT, Silk Scientific Corporation.

Spackman, P. R., M. J. Turner, J. J. McKinnon, S. K. Wolff, D. J. Grimwood, D. Jayatilaka, and M. A. Spackman. 2021. "Crystalexplorer: A Program for Hirshfeld Surface Analysis, Visualization and Quantitative Analysis of Molecular Crystals." *Journal of Applied Crystallography* 54: 1006–11. doi:10.1107/S1600576721002910.

Sykes, R. A., P. McCabe, F. H. Allen, G. M. Battle, I. J. Bruno, and P. A. Wood. 2011. "New Software for Statistical Analysis of Cambridge Structural Database Data." *Journal of Applied Crystallography* 44: 882–6.

Toby, B. H., and R. B. Von Dreele. 2013. "GSAS II: The Genesis of a Modern Open Source All Purpose Crystallography Software Package." *Journal of Applied Crystallography* 46: 544–9.

van de Streek, J., and M. A. Neumann. 2014. "Validation of Molecular Crystal Structures from Powder Diffraction Data with Dispersion-Corrected Density Functional Theory (DFT-D)." *Acta Crystallographica Section B: Structural Science, Crystal Engineering and Materials* 70: 1020–32.

Wang, J., B. H. Toby, P. L. Lee, L. Ribaud, S. M. Antao, C. Kurtz, M. Ramanathan, R. B. Von Dreele, and M. A. Beno. 2008. "A Dedicated Powder Diffraction Beamline at the Advanced Photon Source: Commissioning and Early Operational Results." *Review of Scientific Instruments* 79: 085105.

Wavefunction, Inc. 2022. *Spartan '20. V. 1.1.4*. Irvine CA, Wavefunction Inc.

Wheatley, A. M., and J. A. Kaduk. 2019. "Crystal Structures of Ammonium Citrates." *Powder Diffraction* 34: 35–43.